Research Paper

# Carbon nanotubes covalent combined with graphitic carbon nitride for photocatalytic hydrogen peroxide production under visible light

Shen Zhao[a], Tao Guo[a,b,c], Xia Li[a,d], Tongguang Xu[e], Bo Yang[b,c], Xu Zhao[a,d,*]

[a] Key Laboratory of Drinking Water Science and Technology, Research Center for Eco-Environmental Sciences, Chinese Academy of Sciences, Beijing 100085, China
[b] Department of Environmental Engineering, College of Chemistry and Environmental Engineering, Shenzhen University, Shenzhen, 518060, China
[c] Shenzhen Key Laboratory of Environmental Chemistry and Ecological Remediation, Shenzhen University, Shenzhen, 518060, China
[d] University of Chinese Academy of Sciences, Beijing, 100049, China
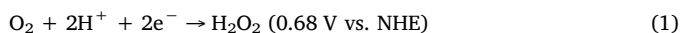[e] Beijing Third Class Tobacco Supervision Station, Beijing 101121, China

## ARTICLE INFO

## ABSTRACT

The carbon nanotubes (CNTs) have been combined with graphitic carbon nitride (g-$C_3N_4$) through the amidation reaction. The hybrid catalyst of g-$C_3N_4$-CNTs with well-defined and stable structure exhibits efficient catalytic performance (32.6 $\mu$mol h$^{-1}$) for photocatalytic $H_2O_2$ production in the presence of formic acid under visible light. The value of electron transfer during the oxygen reduction reaction (ORR) process obtained from the Koutecky-Levich plot for g-$C_3N_4$-CNTs (n = 1.96) is higher than that for g-$C_3N_4$ (n = 1.29), suggesting that the CNTs covalent combined with g-$C_3N_4$ can promote the electrons generation. The *p*-benzoquinone (PBQ) scavenger experiments, the electron spin resonance (ESR) signal and quantitative experiment of $\cdot O_2^-$ results reveal that the negative shifts of the conduction band (CB) level from g-$C_3N_4$ to g-$C_3N_4$-CNTs can enhance the single-electron reduction of $O_2$ to $\cdot O_2^-$ and further promote the sequential two-step single-electron $O_2$ reduction reaction to $H_2O_2$.

## 1. Introduction

As a promising high-energy product, hydrogen peroxide ($H_2O_2$) can act as both oxidatnt and reductant in organic synthesis, environmental remediation, disinfection and fuel cells, producing $H_2O$ as the sole byproduct [1]. Nowadays, many methods including the anthraquinone method [2a], the direct synthesis from $H_2$ and $O_2$ [2b], the alcohols oxidation method [2c] and electrochemical synthesis [2d] have been adopted to produce $H_2O_2$. However, the above methods have two shortcomings: 1) large amounts of energy and organic solvents have been consumed; 2) organic impurities may contaminate the formed $H_2O_2$ and increase the difficulty of extraction. Therefore, an efficient, energy-saving and green method to produce $H_2O_2$ is highly desired.

$$O_2 + 2H^+ + 2e^- \rightarrow H_2O_2 \ (0.68 \text{ V vs. NHE}) \tag{1}$$

$$O_2 + e^- \rightarrow \cdot O_2^- \ (-0.13 \text{ V vs. NHE}) \tag{2}$$

$$\cdot O_2^- + 2H^+ + e^- \rightarrow H_2O_2 \ (1.44 \text{ V vs. NHE}) \tag{3}$$

The photocatalytic $H_2O_2$ production through proton-coupled electron transfer (PCET) can meet the above requirement because it needs only water ($H_2O$), dioxygen ($O_2$) and light [3]. Among the

semiconductor catalysts utilized in the photocatalytic $H_2O_2$ production, graphitic carbon nitride (g-$C_3N_4$)-based catalysts exhibit two advantages compared with the metal oxide-based catalysts: 1) g-$C_3N_4$-based catalysts can promote the photocatalytic $H_2O_2$ production under visible light; 2) g-$C_3N_4$-based catalysts can stabilize the formed $H_2O_2$ under light irradition [4]. Generally, the photocatalytic $H_2O_2$ production over g-$C_3N_4$-based catalysts can process either a direct two-electron $O_2$ reduction (Eq. (1)) [5] or a sequential two-step single-electron $O_2$ reduction (Eqs. (2) and (3)) [6]. The positive shift of the conduction band (CB) level in g-$C_3N_4$-based catalysts can enhance the direct two-electron $O_2$ reduction to $H_2O_2$ [5]. However, the strategy of promoting the sequential two-step single-electron $O_2$ reduction to $H_2O_2$ over g-$C_3N_4$-based catalysts remains unknown. Developing the strategy of promoting the sequential two-step single-electron $O_2$ reduction to $H_2O_2$ over g-$C_3N_4$-based catalysts is therefore demanded.

During photocatalysis process, the electron transfer materials such as the metal complex and carbonaceous nanomaterials immobilized onto g-$C_3N_4$ can accept the photoinduced electrons from the CB level of g-$C_3N_4$ and increase the activity of reduction reaction [7]. As one type of carbonaceous nanomaterials, carbon nanotubes (CNTs) with $\pi$-conjugative structure are capable of accepting, transporting and storing

electrons [8]. Therefore, introducing the CNTs in g-C$_3$N$_4$ to form the hybrid catalyst of g-C$_3$N$_4$-CNTs can enhance the photoinduced electrons generation and further increase the activity of reduction reaction. Although the CNTs has been successfully combined with g-C$_3$N$_4$ based on the electrostatic interaction [9], the effective electronic connection between CNTs and g-C$_3$N$_4$ is far from trivial and cannot transfer the electron effectively [10]. Therefore, the development of covalent combining CNTs with g-C$_3$N$_4$ to enhance the interaction between them is highly desirable.

Herein, the graphene-like g-C$_3$N$_4$ nanosheets have been prepared by a facile dicyandiamide-blowing method with NH$_4$Cl as the gas template [11], which have larger amounts of primary amine (−NH$_2$) groups than the g-C$_3$N$_4$ prepared by the thermally decomposition of dicyandiamide (Fig. S1). The CNTs have been covalent combined with g-C$_3$N$_4$ through the amidation reaction [12]. The hybrid catalyst of g-C$_3$N$_4$-CNTs with well-defined and stable structure exhibits efficient catalytic performance (32.6 μmol h$^{-1}$) for photocatalytic H$_2$O$_2$ production in the presence of formic acid under visible light. The catalytic and characterization results reveal that the covalent combination of CNTs and g-C$_3$N$_4$ can enhance the single-electron reduction of O$_2$ to ·O$_2^-$ and further promote the sequential two-step single-electron O$_2$ reduction reaction to H$_2$O$_2$.

## 2. Experimental section

### 2.1. Chemicals

Dicyandiamide, ammonium chloride (NH$_4$Cl), nitric acid (HNO$_3$, 65 wt.%), thionyl chloride (SOCl$_2$), formic acid, *N,N*-dimethylformamide (DMF), acetonitrile and nitro blue tetrazolium (NBT) were purchased from Alfa Asear company and used as received without further purification. CNTs (MWCNTs, purity > 95%) were purchased from Chengdu Organic Chemicals Co. Ltd, Chinese Academy of Sciences. 5,5-dimethyl-1-pyrroline (DMPO) and 2,2,6,6-tetramethylpiperidine-1-oxyl (TEMPO) were purchased from Sigma-Aldrich company.

### 2.2. Preparation of g-C$_3$N$_4$ [11]

2.00 g of dicyandiamide and 10.00 g of NH$_4$Cl were fully mixed. The mixture was placed in a crucible and heated at 550 °C for 4 h at a rate of 3 °C min$^{-1}$. Then, the crucible was cooled to room temperature naturally. The resulting yellow product was collected and ground into fine powder for further use. Based on the TGA and EA analysis, the formula of g-C$_3$N$_4$ was determined to be C$_{2.53}$N$_4$H$_{2.03}$O$_{0.51}$. For comparison, the g-C$_3$N$_4$-DCA was been prepared by thermally decomposing dicyandiamide at 550 °C in a crucible with a cover for 4 h in static air with a ramp rate of 3 °C min$^{-1}$.

### 2.3. Preparation of CNTs-COOH [13]

0.30 g of CNTs was loaded on the porous SiO$_2$ griddle of a 30 ml silica crucible and then placed into a 50 ml Teflon-vessel, at the bottom of which 5 ml HNO$_3$ was added previously. Subsequently, the Teflon vessel was sealed in the autoclave and then moved to the oven for steaming at the temperature of 180 °C within 4 h. After the steaming treatment, cooled down the autoclave to the room temperature and took the silica crucible out of the Teflon vessel into a clean beaker, in which washed the CNTs-COOH with distilled water and ethanol by in-situ filtration. Finally, the silica crucible was transferred to the oven for drying at 60 °C and the formed solid black cakes could be collected.

### 2.4. Preparation of CNTs-COCl [14]

0.05 g of CNTs-COOH was stirred in a mixture of 10 ml SOCl$_2$ and 1 ml DMF at approximately 80 °C for 24 h. Then, the mixture was

isolated by vacuum filtration through a PTFE membrane (pore size: 0.2 mm), washed with acetonitrile. Usually, the CNTs-COCl was used almost immediately after isolation in the next reaction step in order to avoid the hydrolysis of the formed chloroanhydride.

### 2.5. Preparation of g-C$_3$N$_4$-CNTs

g-C$_3$N$_4$ (1.00 g) was dispersed in 30 ml acetonitrile, and CNTs-COCl (0.05 g) was added. The reaction mixture was stirred at 80 °C for 24 h. The hybrid catalyst of g-C$_3$N$_4$-CNTs was centrifugated, washed by water, and then dried at 60 °C in air. Based on the TGA and EA analysis, the formula of g-C$_3$N$_4$-CNTs was determined to be C$_{2.77}$N$_4$H$_{1.97}$O$_{0.61}$ (4.58 wt.% CNTs). For comparison, g-C$_3$N$_4$-CNTs-IMP based on the electrostatic interaction has been prepared through the impregnation method with the same CNTs weight percentage as g-C$_3$N$_4$-CNTs based on covalent interaction.

### 2.6. Photocatalytic evaluation

The photocatalytic activities were evaluated by the activation of oxygen under light irradiation (λ ≥ 400 nm). A 300 W Xenon lamp (Perfect Light Company, Beijing) was chosen as light source. During each photocatalytic performance, 0.10 g of catalyst was dispersed into 100 ml of formic acid/water mixture (5/95 v/v) in a container (1 g L$^{-1}$ catalyst). After that, the dispersion was stirred in the dark for 60 min to ensure the adsorption-desorption equilibrium among the catalyst, dissolved oxygen and water before light irradiation. During the irradiation, 1.5 ml of the suspensions was taken from the reaction cell at given time intervals, and then filtrated to remove the catalysts. The concentrations of H$_2$O$_2$ generated were determined by iodometric titration [3b]. After completion of the reaction, the catalysts can be recovered by centrifugation, washed with water, and dried at 60 °C in air. To investigate the decomposition behavior of H$_2$O$_2$ over the photocatalysts, a sample of 1 g L$^{-1}$ was dispersed in H$_2$O$_2$ solution (initial concentration: 1 mM) and irradiated for 60 min under continuous stirring.

### 2.7. Rotating disk electrode (RDE) measurements

The measurements were performed on a Pine AFMSRXE 1523 advanced electrochemical system with a three-electrode cell using an Ag/AgCl electrode and a Pt wire electrode as the reference and counter electrode, respectively [15a]. The working electrode was prepared as follows: catalysts (50 mg) were dispersed in EtOH (2 ml) containing Nafion (50 mg) by ultrasonication. The slurry (20 μl) was put onto a Pt disk electrode and dried at room temperature. The LSV were obtained in an O$_2$-saturated 0.1 M phosphate buffer solution (pH 7) with a scan rate 10 mV s$^{-1}$ after O$_2$ bubbling for 5 min. The average number of electrons (n) involved in the overall O$_2$ reduction can be estimated by the linear regression of the plots using the following equations:

$$j^{-1} = j_k^{-1} + B^{-1}\omega^{-1/2} \tag{4}$$

$$B = 0.2nF\nu^{-1/6}CD^{2/3} \tag{5}$$

*j* is the current density, $j_k$ is the kinetic current density, $\omega$ is the rotating speed (rpm), *F* is the Faraday constant (96,485 C mol$^{-1}$), $\nu$ is the kinetic viscosity of water (0.01 cm$^2$ s$^{-1}$), *C* is the bulk concentration of O$_2$ in water (1.26 × 10$^{-3}$ mol cm$^{-3}$), and *D* is the diffusion coefficient of O$_2$ (2.7 × 10$^{-5}$ cm$^2$ s$^{-1}$), respectively [15b].

### 2.8. ·O$_2^-$ radical examination

·O$_2^-$ was examined by a Bruker model electron spin resonance (ESR) A300-10/12 spectrometer equipped with a quanta-Ray Nd: YAG laser system employing 5,5-dimethyl-ʟ-pyrroline-*N*-oxide (DMPO) as the spin trapper. Typically, catalyst (0.10 g) was added to a methanol/
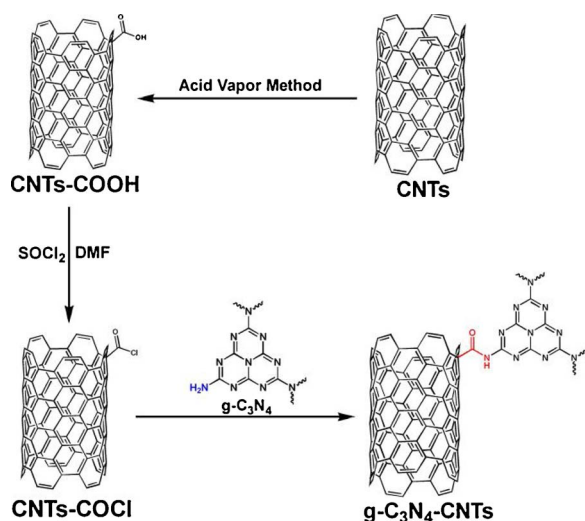
**Fig. 1.** Preparation process of g-C₃N₄-CNTs.

water mixture (9/1 v/v, 100 ml) containing DMPO (0.125 mmol) within a container. After O₂ bubbling for 10 min, the container was photo irradiated for 3 min. The catalyst was recovered by filtration, and the solution was subjected to analysis at room temperature.

### 2.9. ·O₂⁻ radical examination [16]

In order to quantify the $\cdot O_2^-$ concentration, nitro blue tetrazolium (NBT) has been chosen as a $\cdot O_2^-$ radical scavenger because NBT can be reduced by $\cdot O_2^-$ radicals and formed purple formazan, which was insoluble in water. The photocatalytic activities were evaluated by the activation of oxygen under light irradiation ($\lambda \geq 400$ nm). A 300 W Xenon lamp (Perfect Light Company, Beijing) was chosen as light source. During each photocatalytic performance, 0.10 g of catalyst was added to a formic acid/water mixture (5/95 v/v, 100 ml) containing NBT (0.02 mM) within a container (1 g L⁻¹ catalyst). After that, the dispersion was stirred in the dark for 60 min to ensure the adsorption-desorption equilibrium among the catalyst, dissolved oxygen and water before light irradiation. During the irradiation, 3.0 ml of the suspensions was taken from the reaction cell at given time intervals, and then filtrated to remove the catalysts. The concentration of $\cdot O_2^-$ radicals was determined by the degradation of NBT, measured by the absorbance change at the wavelength of 259 nm. The mole ratio of generated $\cdot O_2^-$ radicals and degraded NBT was 4: 1 according to the following equation:
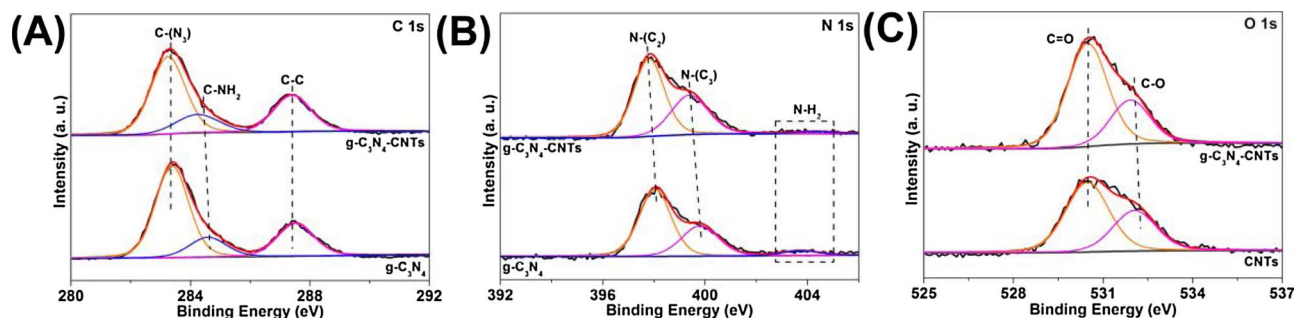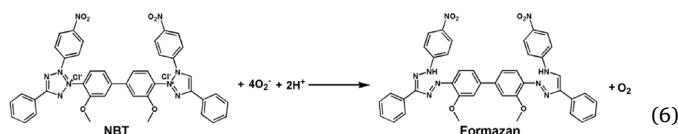


(6)

### 2.10. Photogenerated electrons demonstration [17]

2,2,6,6-Tetramethylpiperidine-1-oxyl (TEMPO) was examined by a Bruker model electron spin resonance (ESR) A300-10/12 spectrometer equipped with a quanta-Ray Nd: YAG laser system. The reduction of TEMPO by electrons produces an ESR silent molecule, TEMPOH, and leads to the reduction of intensity and flatting of ESR spectra. Therefore, the consumption of TEMPO demonstrates that reactive electrons are generated during photo-excitation. Typically, catalyst (0.10 g) was added to a formic acid/water mixture (5/95 v/v, 100 ml) containing TEMPO (0.02 mM) within a container. After stirring for 10 min, the mixture was photo irradiated for 3 min. The catalyst was recovered by filtration, and the solution was subjected to analysis at room temperature.

## 3. Results and discussion

### 3.1. Covalent combination of CNTs and g-C₃N₄

The graphene-like g-C₃N₄ nanosheets have been prepared by a facile dicyandiamide-blowing method with NH₄Cl as the gas template [11], which have larger amounts of primary amine (−NH₂) groups than the g-C₃N₄ prepared by the thermally decomposition of dicyandiamide (Fig. S1). As shown in Fig. 1, the oxidation of CNTs to CNTs-COOH have been achieved through the acid vapor method [13]. Then, the CNTs-COOH have been transformed to CNTs-COCl by refluxing with an excess of thionyl chloride (SOCl₂) in the presence of a small amount of N,N-dimethylformamide (DMF) [14]. Finally, the acyl chloride (−COCl) groups of CNTs-COCl can react with the −NH₂ groups of g-C₃N₄ to form the amide (−CONH−) groups [12]. In this way, the CNTs have been covalent combined with g-C₃N₄ to form the hybrid catalyst of g-C₃N₄-CNTs for photocatalytic H₂O₂ production.

### 3.2. Characterization of g-C₃N₄-CNTs

Fig. 2 shows the C 1s, N 1s, and O 1s XPS spectra of g-C₃N₄, CNTs, and g-C₃N₄-CNTs. As shown in Fig. 2A, XPS peaks of C 1s for g-C₃N₄ and g-C₃N₄-CNTs can be fitted with three peaks at binding energies of around 283.3, 284.4 and 287.5 eV, which are ascribed to the tertiary carbon C−N₃ groups, the C−NH₂ groups and the C−C groups, respectively [18]. The area ratios of the C−C groups peaks to the tertiary carbon C−N₃ peaks are 0.39 and 0.51 for g-C₃N₄ and g-C₃N₄-CNTs; while the area ratios of the C−NH₂ groups peaks to the tertiary carbon C−N₃ peaks are 0.30 and 0.24 for g-C₃N₄ and g-C₃N₄-CNTs. The increase of the C−C groups and the decrease of the C−NH₂ groups support the CNTs have been covalent combined with g-C₃N₄. Nevertheless, the XPS peaks of N 1s (Fig. 2B) for g-C₃N₄ can be fitted with three peaks at 398.1, 399.8, and 403.7 eV, which are assigned to the N-(C₂), N-(C₃), and −NH₂, respectively [5,6][5c,6b]. However, the g-C₃N₄-CNTs only exhibits two peaks at 397.8 and 399.4 eV corresponding to N-(C₂) and N-(C₃). The disappearance of −NH₂ peak indicates that the −NH₂ groups of g-C₃N₄ react with the acyl chloride (−COCl) groups of CNTs-



**Fig. 2.** C 1s (A), N 1s (B), and O 1s (c) XPS spectra of g-C₃N₄, CNTs and g-C₃N₄-CNTs.

COCl to form the amide groups (−CONH−) during the covalent combination of CNTs with g-$C_3N_4$. XPS peaks of O 1s (Fig. 2C) for CNTs and g-$C_3N_4$-CNTs can be fitted with two peaks at binding energies of around 530.5 and 532.0 eV, which are ascribed to the C=O groups and the C−O groups, respectively [19]. The area ratios of these two peaks are 1.72 and 2.39 for CNTs and g-$C_3N_4$-CNTs. The increase of the C=O groups support the presence of the −CONH− groups in g-$C_3N_4$-CNTs.

The above XPS results confirm the CNTs have been covalent combined with g-$C_3N_4$ through the amidation reaction. The XRD patterns of g-$C_3N_4$, CNTs and g-$C_3N_4$-CNTs are shown in Fig. S2. The g-$C_3N_4$ has two distinct diffraction peaks at 13.1° and 27.6°, which correspond to the graphitic materials as the (100) and (002) diffraction planes in JCPDS 87-1526 [20]. The diffraction peak at 26.4° in CNTs can be attributed to the graphite-like structure (002) of the CNTs [9a,b]. For g-$C_3N_4$-CNTs, only the diffraction peaks at 13.1° and 27.6° assigned to the (100) and (002) diffraction planes of g-$C_3N_4$ have been observed, indicating that the covalent combined CNTs have been highly dispersed on g-$C_3N_4$ [9c,d]. Fig. S3 shows the IR spectra of g-$C_3N_4$, CNTs and g-$C_3N_4$-CNTs. No distinct changes can be observed for g-$C_3N_4$-CNTs in comparison to g-$C_3N_4$, which is consistent with the reported results [9c,d]. The sharp peak at 810 $cm^{-1}$ is originated from the breathing mode of the *tri*-s-triazine units of g-$C_3N_4$. The peaks in the region from 900 to 1800 $cm^{-1}$ are attributed to typical bands of aromatic CN heterocycles containing either trigonal N(-C)$_3$ (full condensation) or bridging C−NH−C units (partial condensation), evidencing the formation of extended network of C−N−C bonds [9c,d]. In addition, the broad peaks at around 3100–3400 $cm^{-1}$ are mainly due to the −$NH_2$ groups of the adsorbed $H_2O$ from air, which become weaker after covalent combination [21], indicating the decreased content of surface −$NH_2$ groups in g-$C_3N_4$-CNTs. $CO_2$ temperature programmed desorption ($CO_2$-TPD) has been performed to investigate the content of −$NH_2$ groups in g-$C_3N_4$ and g-$C_3N_4$-CNTs as the −$NH_2$ groups can act as Lewis base sites and adsorb slightly acidic $CO_2$ molecules [22]. Fig. S4 shows the peak area of g-$C_3N_4$-CNTs is smaller than that of g-$C_3N_4$. Furthermore, the zeta potentials of aqueous suspension of g-$C_3N_4$ and g-$C_3N_4$-CNTs have been measured because the −$NH_2$ groups with the free lone pair electrons on nitrogen atoms can act as proton acceptors and acquire positive surface charges [23]. Fig. S5 shows the zeta potential of g-$C_3N_4$-CNTs (−18.6 mV) is more negative than that of g-$C_3N_4$ (−15.2 mV). The above IR, $CO_2$-TPD and zeta potential results reveal the significant decrease of −$NH_2$ groups in g-$C_3N_4$ after covalent combination, confirming the reaction between the −$NH_2$ groups of g-$C_3N_4$ and the carboxyl groups of CNTs. The nitrogen adsorption-

desorption isotherms and pore size distribution patterns for g-$C_3N_4$ and g-$C_3N_4$-CNTs are shown in Fig. S6. The isotherms for g-$C_3N_4$ and g-$C_3N_4$-CNTs (Fig. S6A) show type IV isotherm with a type H3 hysteresis loop. These two catalysts present two peaks centered at 3.8 nm and 41.9 nm in a broad pore-size distribution curve (1–132 nm) in Fig. S6B, which are probably attributed to the inner cavity diameter of the CNTs and the pores formed in the assembled 3D matrix, respectively [9c]. The surface area, pore volume and pore diameter of g-$C_3N_4$ and g-$C_3N_4$-CNTs are shown in Table S1. Compared with g-$C_3N_4$, the decrease in these values of g-$C_3N_4$-CNTs is due to the mesopores of the covalent combined CNTs have been blocked by g-$C_3N_4$ [9d]. Thermogravimetry analysis (TGA) curves for g-$C_3N_4$, CNTs and g-$C_3N_4$-CNTs are shown in Fig. S7. The total weight loss of g-$C_3N_4$ is 99.85% between 30 and 800 °C due to the direct thermal decomposition of g-$C_3N_4$. For CNTs, the weight loss in the range of 30–800 °C range (27.23%) corresponds to the oxidative degradation of the CNTs [12]. Combining the TGA and EA analysis (Table S2), the molecular formulas of g-$C_3N_4$ and g-$C_3N_4$-CNTs can be given as $C_{2.53}N_4H_{2.03}O_{0.51}$ and $C_{2.77}N_4H_{1.97}O_{0.61}$ (4.58 wt. % CNTs).

Fig. S8 is the TEM images of the g-$C_3N_4$, which exhibit sheet-like structure. The TEM images of the g-$C_3N_4$-CNTs are shown in Fig. 3. It is clear that the tube-like CNTs are highly dispersed on g-$C_3N_4$ [9a,d]. The HR-TEM image of g-$C_3N_4$-CNTs (Fig. 3D) is quite different from that of g-$C_3N_4$ (Fig. S8D), which shows that the CNTs and the g-$C_3N_4$ have been effectively combined together after covalent combination [9b,c].

The above characterization results confirm that the CNTs has been covalent combined with g-$C_3N_4$ to form the hybrid catalyst of g-$C_3N_4$-CNTs. Furthermore, the catalytic performanc of g-$C_3N_4$-CNTs should be investigated.

### 3.3. Catalytic performance of g-$C_3N_4$-CNTs

The photocatalytic $H_2O_2$ production over various catalysts has been conducted and monitored in an $O_2$-equilibrated conditions and light irradiation (λ ≥ 400 nm) in the presence of 5 vol.% formic acid at 25 °C. To investigate the role of formic acid in the photocatalytic $H_2O_2$ production, the photocatalytic $H_2O_2$ production over g-$C_3N_4$-CNTs in the presence of 5 vol.% methanol or formic acid has been performed (Fig. S9). The catalytic performance of g-$C_3N_4$-CNTs with 5 vol.% methanol (23.1 μmol in 60 min) is lower than that of g-$C_3N_4$-CNTs with 5 vol.% formic acid (48.7 μmol in 60 min). The pH values of the methanol/water (5/95) and formic acid/water (5/95) solutions are 7.2 and 1.7 respectively. The decreasing pH of the reaction solution can
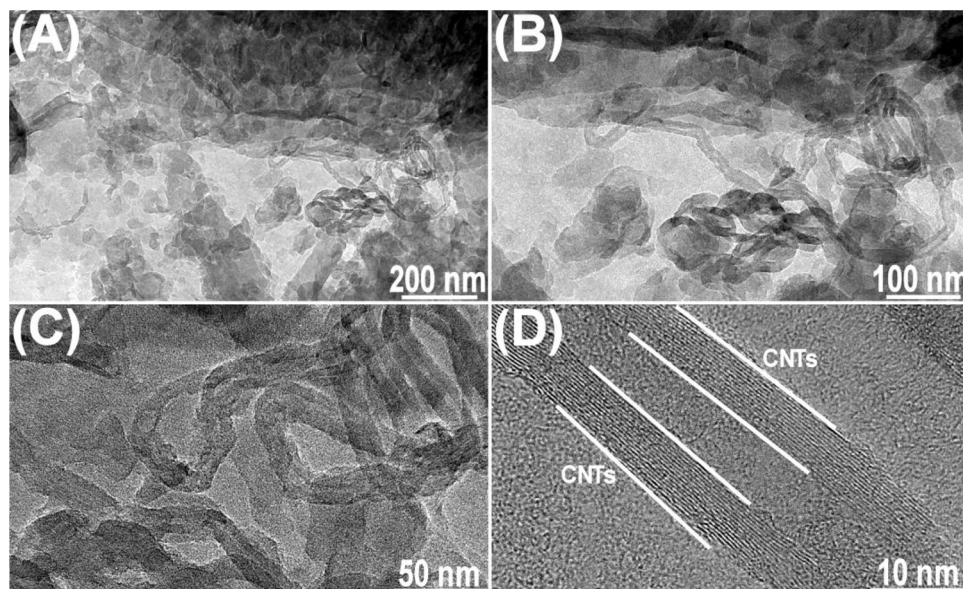


**Fig. 3.** TEM images (A–D) of g-$C_3N_4$-CNTs.

accelerate the photocatalytic $H_2O_2$ production under visible light irradiation [3b]. Therefore, formic acid works as not only a good electron donor but also as a pH-regulating agent. It has been reported that the formic acid can be oxidized to the carbon dioxide ($CO_2$) with almost stoichiometric production of $H_2O_2$ with molar ratio of 1:1 under similar reaction conditions [3b]. The equation of the photocatalytic $H_2O_2$ production in the presence of formic acid can be presented as Eq. (7):

$$O_2 + HCOOH \rightarrow H_2O_2 + CO_2 \quad \Delta_r G^0 = -153.4 \text{ kJ mol}^{-1} \tag{7}$$
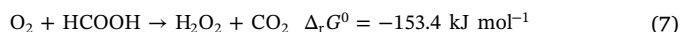
As shown in Fig. 4A, the $H_2O_2$ can be rapidly generated over g-$C_3N_4$-CNTs and the amounts of formed $H_2O_2$ can reach 48.7 μmol in 60 min. The catalytic performance of individual g-$C_3N_4$ (15.2 μmol in 60 min) or CNTs (2.1 μmol in 60 min) is lower than that of g-$C_3N_4$-CNTs. For comparison, g-$C_3N_4$-CNTs-IMP based on the electrostatic interaction has been prepared through the impregnation method with the same CNTs weight percentage as g-$C_3N_4$-CNTs based on covalent interaction. g-$C_3N_4$-CNTs-IMP shows lower catalytic performance (18.1 μmol in 60 min). The reaction cannot proceed in the absence of catalyst (< 0.1 μmol in 60 min). The photocatalytic $H_2O_2$ production over g-$C_3N_4$ and g-$C_3N_4$-CNTs has been performed under $N_2$- and $O_2$-equilibrated conditions to investigate the role of $O_2$ in the photocatalytic $H_2O_2$ production (Fig. S10). Generally, the photoexcited conduction band (CB) electrons can be scavenged by dissolved $O_2$ under $O_2$-equilibrated conditions but the protons should uptake the electrons in the absence of $O_2$ ($N_2$-equilibrated conditions) [3c]. Under $N_2$-equilibrated conditions, no $H_2O_2$ can be formed over both g-$C_3N_4$ and g-$C_3N_4$-CNTs, confirming that the $H_2O_2$ is generated through the $O_2$ reduction. The effect of initial CNTs dosage (2.5 wt.%, 5 wt.% and 7.5 wt.%) have been investigated. As shown in Fig. S11, g-$C_3N_4$-CNTs-5 exhibits higher catalytic performance than g-$C_3N_4$-CNTs-2.5. As the CNTs can act as an electron reservoir to trap electrons immigrated from photoexcited g-$C_3N_4$, increasing the loading of CNTs from 2.5 wt.% to 5 wt.% can hinder the charge recombination and improve the activity of g-$C_3N_4$-CNTs toward photocatalytic $H_2O_2$ production under visible light.

However, the further loading of CNTs from 5 wt.% to 7.5 wt.% decrease the photocatalytic performance. This is due to the competitive light absorption of CNTs to g-$C_3N_4$ while no effective electron-transfer channels could be formed between the unoccupied CNTs and g-$C_3N_4$ [9c,d]. Fig. S12 shows the g-$C_3N_4$-DCA prepared by the thermally decomposition of dicyandiamide shows lower catalytic performance (2.8 μmol in 60 min) than g-$C_3N_4$ through dicyandiamide-blowing method with $NH_4Cl$ as the gas template (15.2 μmol in 60 min). The reason is that g-$C_3N_4$ has larger amounts of $-NH_2$ groups that are active for photocatalytic $H_2O_2$ production than g-$C_3N_4$-DCA [5c,6b].

$$[H_2O_2] = \frac{K_f}{K_d}(1 - e^{K_d t}) \tag{8}$$

The formation and decomposition of $H_2O_2$ over catalysts proceeds through two competitive pathways owing to the thermodynamic instability of $H_2O_2$ at room temperature [3a,24]. The $K_f$ and $K_d$ values have been estimated by fitting the data in Fig. 4A according to Eq. (8) and the results are presented in Fig. 4B [25]. In order to investigate the stability of different catalysts, the reaction time has been extended to 240 min. The maximum amounts of formed $H_2O_2$ over g-$C_3N_4$-CNTs, g-$C_3N_4$-CNTs-IMP and g-$C_3N_4$ can be obtained as 130.2, 53.8 and 42.1 μmol in 240 min, respectively (Fig. 4C), which gives the $H_2O_2$ formation rate of 32.6, 13.5 and 10.5 μmol h$^{-1}$ for g-$C_3N_4$-CNTs, g-$C_3N_4$-CNTs-IMP and g-$C_3N_4$ (Table S3). The values of $K_f$ obtained from the photocatalytic $H_2O_2$ production over different catalysts (Fig. 4B) decrease in the following order: g-$C_3N_4$-CNTs (1.0806 μmol min$^{-1}$) > g-$C_3N_4$-CNTs-IMP (0.4505 μmol min$^{-1}$) > g-$C_3N_4$ (0.4382 μmol min$^{-1}$) > CNTs (0.0438 μmol min$^{-1}$) > None (0.0042 μmol min$^{-1}$), which is consistent with the above $H_2O_2$ formation rate of different catalysts (Fig. 4B). Furthermore, the values of $K_d$ obtained from the photocatalytic $H_2O_2$ decomposition over different catalysts (Fig. S13) increases in the following order: None (0.0072 min$^{-1}$) < CNTs (0.0091 min$^{-1}$) < g-$C_3N_4$-CNTs (0.0149 min$^{-1}$) < g-$C_3N_4$ (0.0203 min$^{-1}$) < g-$C_3N_4$-CNTs-IMP (0.0234 min$^{-1}$). The above results confirm that the covalent combination of CNTs and g-$C_3N_4$ can stabilize the
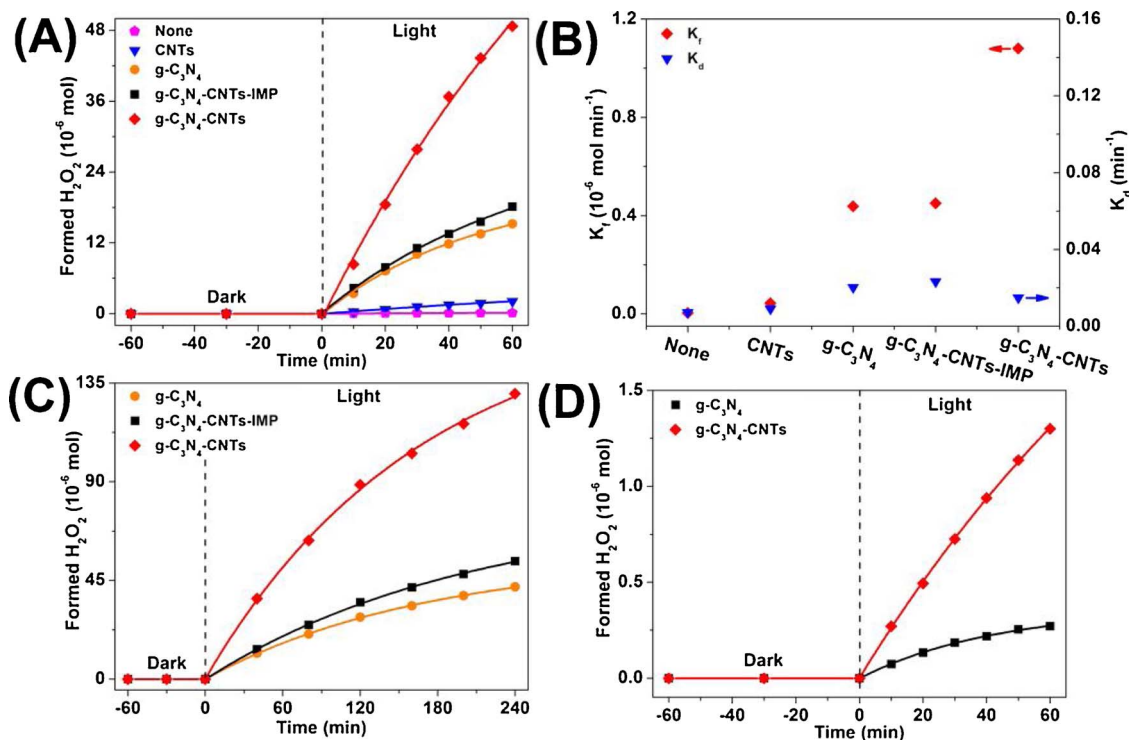


**Fig. 4.** Photocatalytic $H_2O_2$ formation over different catalysts in 60 min (A and B). Reaction conditions: formic acid/water mixture (5/95 v/v, 100 ml), catalyst (0.10 g, 1 g L$^{-1}$), $O_2$-equilibrated, $\lambda \geq 400$ nm, 25 °C. Photocatalytic $H_2O_2$ formation over g-$C_3N_4$-CNTs, g-$C_3N_4$-CNTs-IMP and g-$C_3N_4$ in 240 min (C). Reaction conditions: formic acid/water mixture (5/95 v/v, 100 ml), catalyst (0.10 g, 1 g L$^{-1}$), $O_2$-equilibrated, $\lambda \geq 400$ nm, 25 °C. Photocatalytic $H_2O_2$ formation over g-$C_3N_4$-CNTs in the absence of electron donor (D). Reaction conditions: water (100 ml), catalyst (0.10 g, 1 g L$^{-1}$), $O_2$-equilibrated, $\lambda \geq 400$ nm, 25 °C.

formed $H_2O_2$ under light irradiation. Above all, the covalent combination of CNTs and g-$C_3N_4$ can enhance the photocatalytic $H_2O_2$ production.

Under similar reaction conditions over the g-$C_3N_4$-based catalysts with electron donors, the $H_2O_2$ formation rate (32.6 µmol h$^{-1}$) over g-$C_3N_4$-CNTs is more than those over g-$C_3N_4$ (2.5 µmol h$^{-1}$) [4a], meso g-$C_3N_4$ (3.8 µmol h$^{-1}$) [4b], g-$C_3N_4$-KPO (10.0 µmol h$^{-1}$) [3c], 3DOM g-$C_3N_4$-PW$_{11}$ (10.4 µmol h$^{-1}$) [5c] and g-$C_3N_4$-BDI$_{50}$ (22.2 µmol h$^{-1}$) [26]. In addition, the catalytic performance of g-$C_3N_4$-CNTs (32.6 µmol h$^{-1}$) is higher than those of carbonate-surface modified bimodal size distribution-Au/TiO$_2$ (BM-Au/TiO$_2$-CO$_3^{2-}$, 10.0 µmol h$^{-1}$) [3b] and Au$_{0.2}$/BiVO$_4$ (25.0 µmol h$^{-1}$) [27]. Furthermore, the formed $H_2O_2$ can reach 1.3 µmol in 60 min over g-$C_3N_4$-CNTs without electron donor (Fig. 4D), suggesting the g-$C_3N_4$-CNTs can act as a dual-functional catalyst for both water oxidation (Fig. S14) and oxygen reduction [5c,28]. Therefore, the relative high $H_2O_2$ formation rates among the reported g-$C_3N_4$-based catalysts and the ability of producing $H_2O_2$ without electron donor make g-$C_3N_4$-CNTs a promising catalyst for photocatalytic $H_2O_2$ production.

### 3.4. Structure-catalytic performance relationship of g-$C_3N_4$-CNTs

Photoelectrochemical characterization should be performed to clarify the reason for the efficient activity of g-$C_3N_4$-CNTs. As shown in Fig. S15A, the photo-current density of g-$C_3N_4$-CNTs (0.32 µA cm$^{-2}$) is much larger than that of g-$C_3N_4$ (0.03 µA cm$^{-2}$). Photoelectrochemical impedance spectroscopy (EIS) results are shown in Fig. S15B. The diameter of Nyquist semicircle for g-$C_3N_4$-CNTs is smaller than that of g-$C_3N_4$, which indicates that the g-$C_3N_4$-CNTs composites have lower resistances than g-$C_3N_4$. The emission peak appearing at about 433 nm in photoluminescence (PL) spectra of g-$C_3N_4$ and g-$C_3N_4$-CNTs is attributed to the direct electron-hole recombination of band transition. Compare with g-$C_3N_4$, g-$C_3N_4$-CNTs possess a weaker emission peak (Fig. S16A). The above results reveal that the covalent combination of CNTs and g-$C_3N_4$ can enhance the charge separation of g-$C_3N_4$-CNTs.

Electrochemical rotating disk electrode (RDE) analysis of oxygen reduction reaction (ORR) further investigates the pathway of O$_2$ reduction. Fig. S17 shows the LSV curves of g-$C_3N_4$ and g-$C_3N_4$-CNTs measured on RDE in an O$_2$-saturated 0.1 M phosphate buffer solution (pH 7) at different rotating speeds. Fig. 5A summarizes the Koutecky-Levich plots of the data at −0.9 V vs. Ag/AgCl [15]. The n value for g-$C_3N_4$-CNTs (n = 1.96) is higher than that for g-$C_3N_4$ (n = 1.29), suggesting that the CNTs covalent combined with g-$C_3N_4$ can promote the electrons generation. In order to investigate the generation of photoinduced electrons, electron spin resonance (ESR) analysis with 2,2,6,6-tetramethylpiperidine-1-oxyl (TEMPO) as a spin-trapping reagent has been performed over g-$C_3N_4$ and g-$C_3N_4$-CNTs. The reduction of TEMPO by electrons produces an ESR silent molecule, TEMPOH, and leads to the reduction of intensity and flatting of ESR spectra [17]. As shown in Fig. 5B, when irradiated for 3 min, both g-$C_3N_4$ and g-$C_3N_4$-CNTs caused reduction of the TEMPO signal, suggesting the electron transfer from photoexcited g-$C_3N_4$ or g-$C_3N_4$-CNTs to TEMPO. The consumption of TEMPO demonstrates that reactive electrons are generated during photo-excitation of g-$C_3N_4$ and g-$C_3N_4$-CNTs. The reduction of TEMPO signal intensity caused by g-$C_3N_4$-CNTs is greater than that by g-$C_3N_4$, indicating that higher reducing ability of photoexcited g-$C_3N_4$-CNTs than g-$C_3N_4$. The above results reveal that the CNTs covalent combined with g-$C_3N_4$ can promote the photoinduced electrons generation.

Electron spin resonance (ESR) analysis with 5,5-dimethyl-1-pyrroline N-oxide (DMPO) as a spin-trapping reagent has been performed to confirm the pathway of O$_2$ reduction over different catalysts. Fig. 6A shows the ESR spectra of the solutions recovered after photoreaction over g-$C_3N_4$ and g-$C_3N_4$-CNTs for 3 min. Both solutions exhibit distinctive signals assigned to the DMPO-·O$_2^-$ spin adduct [4b]. The signal intensity for the solution obtained by photoreaction over g-$C_3N_4$-CNTs is stronger than that over g-$C_3N_4$. In order to quantify the ·O$_2^-$ concentration, nitro blue tetrazolium (NBT) has been chosen as a ·O$_2^-$ radical scavenger because NBT can be reduced by ·O$_2^-$ radicals and formed purple formazan, which was insoluble in water [16]. Figs. S18 and 6 B show the evolution of NBT disappearance and the subsequent formation of ·O$_2^-$ radicals during the photocatalytic $H_2O_2$ production over g-$C_3N_4$ and g-$C_3N_4$-CNTs. The ESR signal and quantitative experiment of ·O$_2^-$ results reveal that the CNTs covalent combined with g-$C_3N_4$ can enhance the single-electron reduction of O$_2$ to ·O$_2^-$, suggesting the photocatalytic $H_2O_2$ production over g-$C_3N_4$ and g-$C_3N_4$-CNTs both process through sequential two-step single-electron O$_2$ reduction reaction (Eqs. (2) and (3)) [6]. The scavenger experiments using p-benzoquinone (PBQ) have been performed to investigate the role of ·O$_2^-$. As can be seen from Fig. 6C, the addition of PBQ can actually depress the photocatalytic $H_2O_2$ production over g-$C_3N_4$ and g-$C_3N_4$-CNTs. The PBQ scavenger experiments results confirm that the photocatalytic $H_2O_2$ production over g-$C_3N_4$ and g-$C_3N_4$-CNTs both process through the sequential two-step single-electron O$_2$ reduction reaction and the CNTs covalent combined with g-$C_3N_4$ can enhance the single-electron reduction of O$_2$ to ·O$_2^-$.

The Mott-Schottky plots of g-$C_3N_4$ and g-$C_3N_4$-CNTs at varied frequencies (1.0, 1.5 and 2.0 kHz) exhibit positive slopes (Figs. S19A and B), suggestive of their n-type semiconductor features [29]. A flat band potential of −0.04 V and −0.38 V vs. normal hydrogen electrode (NHE) has been obtained for g-$C_3N_4$ and g-$C_3N_4$-CNTs, respectively [30]. Considering the conduction band (CB) could be 0–0.1 V more negative than the flat band position, the corresponding CB edge of g-



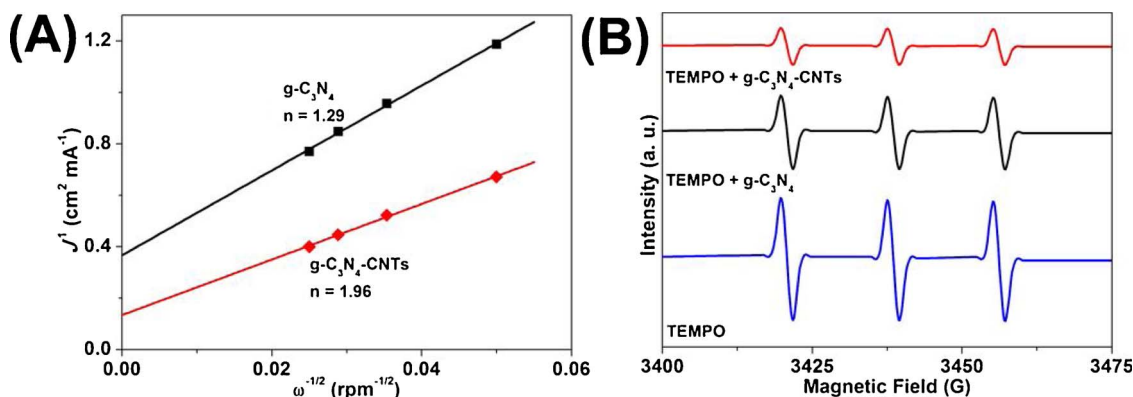**Fig. 5.** Koutecky-Levich plots of the ORR data measured by RDE analysis for g-$C_3N_4$ and g-$C_3N_4$-CNTs (Fig. S17) in a buffered solution (pH 7) at a constant potential of −0.9 V vs Ag/AgCl (A); TEMPO spin trapping ESR technique to investigate the generation of photoinduced electrons during the photoreaction over g-$C_3N_4$ and g-$C_3N_4$-CNTs (B).
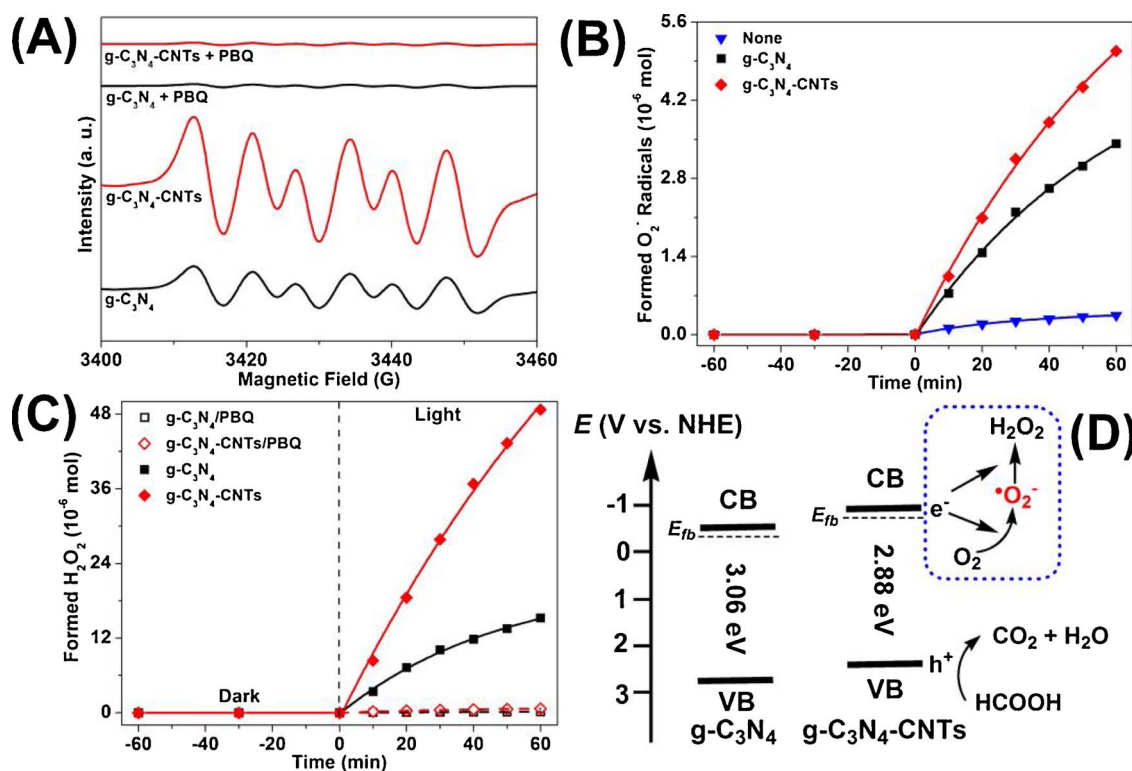
**Fig. 6.** DMPO spin trapping ESR technique to measure $\cdot O_2^-$ generated photoreaction over g-$C_3N_4$ and g-$C_3N_4$-CNTs (A). $\cdot O_2^-$ radicals formation during the photoreaction over g-$C_3N_4$ and g-$C_3N_4$-CNTs (B). Reaction conditions: formic acid/water mixture (5/95 v/v, 100 ml), catalyst (0.10 g, 1 g $L^{-1}$), NBT (0.02 mM), $O_2$-equilibrated, λ ≥ 400 nm, 25 °C. The effect of PBQ for the photocatalytic $H_2O_2$ production over g-$C_3N_4$ and g-$C_3N_4$-CNTs (C). Reaction conditions: formic acid/water mixture (5/95 v/v, 100 ml), catalyst (0.10 g, 1 g $L^{-1}$), PBQ (1 mM), $O_2$-equilibrated, λ ≥ 400 nm, 25 °C. Scheme of energy levels and charge transfer pathways of g-$C_3N_4$ and g-$C_3N_4$-CNTs (D).

$C_3N_4$ and g-$C_3N_4$-CNTs has been estimated to be $-0.14$ V and $-0.48$ V vs. NHE, respectively. From the Tauc plots of g-$C_3N_4$ and g-$C_3N_4$-CNTs (Fig. S16C), the band gap of g-$C_3N_4$ and g-$C_3N_4$-CNTs are 3.06 and 2.88 eV, respectively [31]. Combining the Mott-Schottky measurements and Tauc plots results, the valence band (VB) positions of g-$C_3N_4$ and g-$C_3N_4$-CNTs have been estimated as 2.92 V and 2.40 V vs. NHE, respectively.

As shown in Fig. 6D, a negative shift of 0.34 V for the CB level from g-$C_3N_4$ to g-$C_3N_4$-CNTs has been observed. The negative shift of the CB level in g-$C_3N_4$-CNTs can promote the photoinduced generation, which is consistent with the Koutecky-Levich plots results and ESR results for TEMPO [15,17]. Moreover, the CB level in g-$C_3N_4$-CNTs ($-0.48$ V vs. NHE) has sufficient potential difference (0.35 V) from the single-electron reduction of $O_2$ to $\cdot O_2^-$ ($-0.13$ V vs. NHE), confirming the PBQ scavenger experiments, the ESR signal and quantitative experiment of $\cdot O_2^-$ results [6]. Above all, the negative shifts of the CB level from g-$C_3N_4$ to g-$C_3N_4$-CNTs can enhance the single-electron reduction of $O_2$ to $\cdot O_2^-$ and further promote the sequential two-step single-electron $O_2$ reduction reaction to $H_2O_2$.

### 3.5. Recycle of heterogeneous g-$C_3N_4$-CNTs

It is essential to confirm the catalysis of g-$C_3N_4$-CNTs is truly heterogeneous for photocatalytic $H_2O_2$ production. When the reaction time arrives at 30 min, g-$C_3N_4$-CNTs has been removed from the reaction system by filtration, and the reaction is allowed to proceed with the filtrate under the same conditions. As shown in Fig. 7A, no new $H_2O_2$ forms and the formed $H_2O_2$ starts to decompose under the same conditions. The above results confirm that the g-$C_3N_4$-CNTs is truly heterogeneous for photocatalytic $H_2O_2$ production.

To investigate the stability of heterogeneous g-$C_3N_4$-CNTs, the photocatalytic $H_2O_2$ production has been recycled for three times under the same conditions. Fig. 7B shows the catalytic performance is almost

unchanged and the catalyst recovery can reach above 98% even after three times. The XRD and IR results of the fresh and used g-$C_3N_4$-CNTs exhibit almost the same typical peaks (Fig. S20). The TEM results of the used g-$C_3N_4$-CNTs (Fig. S21) indicate that the sheet-like structure and the dispersion of CNTs cluster on g-$C_3N_4$-CNTs are retained after reaction. The EA results in Table S2 also reveal that the composition of the used g-$C_3N_4$-CNTs remains unchanged. The above results indicate that the heterogeneous g-$C_3N_4$-CNTs is catalytic stable.

## 4. Conclusions

In summary, to develop the strategy of promoting the sequential two-step single-electron $O_2$ reduction to $H_2O_2$ over g-$C_3N_4$-based catalysts, the CNTs have been covalent combined with g-$C_3N_4$ through the amidation reaction. The hybrid catalyst of g-$C_3N_4$ with well-defined and stable structure exhibits efficient catalytic performance (32.6 μmol $h^{-1}$) for photocatalytic $H_2O_2$ production in the presence of formic acid under visible light. Three reasons have been presented for the efficient catalytic performance of g-$C_3N_4$-CNTs from the catalytic and characterization results: 1) The value of electron transfer during the ORR process obtained from the Koutecky-Levich plot for g-$C_3N_4$-CNTs (n = 1.96) is higher than that for g-$C_3N_4$ (n = 1.29), suggesting that the CNTs covalent combined with g-$C_3N_4$ can promote the electrons generation; 2) The reduction of ESR signal intensity for TEMPO caused by g-$C_3N_4$-CNTs is greater than that by g-$C_3N_4$, indicating that higher reducing ability of photoexcited g-$C_3N_4$-CNTs than g-$C_3N_4$; 3) the PBQ scavenger experiments, the ESR signal and quantitative experiment of $\cdot O_2^-$ results reveal that the negative shifts of the CB level from g-$C_3N_4$ to g-$C_3N_4$-CNTs can enhance the single-electron reduction of $O_2$ to $\cdot O_2^-$ and further promote the sequential two-step single-electron $O_2$ reduction reaction to $H_2O_2$.
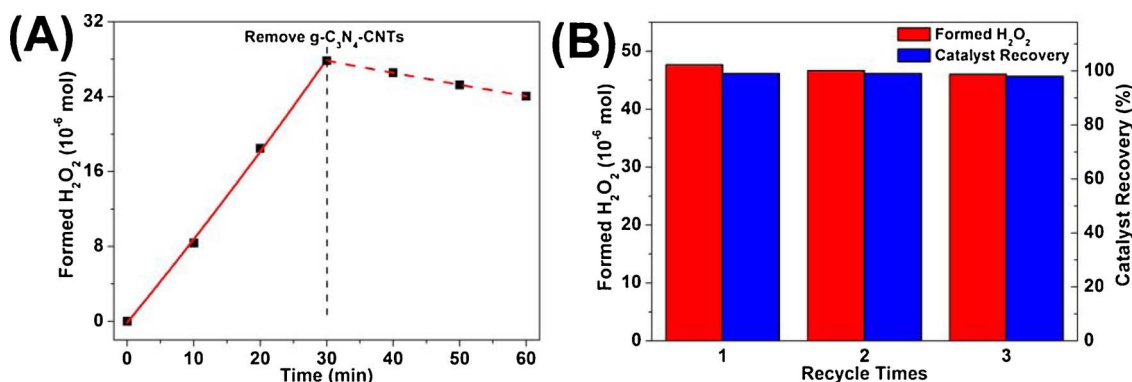
**Fig. 7.** Experiment to prove the heterogeneous nature (A) and the recycle (B) of g-C$_3$N$_4$-CNTs.

## Acknowledgements

## Appendix A. Supplementary data

Supplementary data associated with this article can be found, in the online version, at http://dx.doi.org/10.1016/j.apcatb.2017.11.005.

## References

[1] (a) R. Hage, A. Lienke, Angew. Chem. 118 (2006) 212–229. Angew. Chem. Int. Ed. 45 (2006) 206–222;
(b) J.M. Campos-Martin, G. Blanco-Brieva, J.L.G. Fierro, Angew. Chem. 118 (2006) 7116–7139. Angew. Chem. Int. Ed. 45 (2006) 6962–6984.
[2] (a) F. Sandelin, P. Oinas, T. Salmi, J. Paloniemi, H. Haario, Ind. Eng. Chem. Res. 45 (2006) 986–992;
(b) J.K. Edwards, G.J. Hut Chings, Angew. Chem. 120 (2008) 9332–9338. Angew. Chem. Int. Ed. 47 (2008) 9192–9198;
(c) T. Iwahama, S. Sakaguchi, Y. Ishii, Org. Process Res. Dev. 4 (2000) 94–97;
(d) L.V. Pham, J. Messinger, Biochem. Biophys. Acta 2014 (1837) 1411–1416.
[3] (a) G.H. Moon, W. Kim, A.D. Bokare, N.E. Sung, W. Choi, Energy Environ. Sci. 7 (2014) 4023–4028;
(b) M. Teranishi, R. Hoshino, S.I. Naya, H. Tada, Angew. Chem. 128 (2016) 12965–12969. Angew. Chem. Int. Ed. 55 (2016) 12773–12777;
(c) G.H. Moon, M. Fujitsuka, S. Kim, T. Majima, X. Wang, W. Choi, ACS Catal. 7 (2017) 2886–2895;
(d) S. Thakur, T. Kshetri, N.H. Kim, J.H. Lee, J. Catal. 345 (2017) 78–86.
[4] (a) Y. Shiraishi, S. Kanazawa, Y. Sugano, D. Tsukamoto, H. Sakamoto, S. Ichikawa, T. Hirai, ACS Catal. 4 (2014) 774–780;
(b) Y. Shiraishi, Y. Kofuji, H. Sakamoto, S. Tanaka, S. Ichikawa, T. Hirai, ACS Catal. 5 (2015) 3058–3066.
[5] (a) Y. Shiraishi, S. Kanazawa, Y. Kofuji, H. Sakamoto, S. Ichikawa, S. Tanaka, T. Hirai, Angew. Chem. 126 (2014) 13672–13677. Angew. Chem. Int. Ed. 53 (2014) 13454–13459;
(b) Y. Kofuji, Y. Isobe, Y. Shiraishi, H. Sakamoto, S. Tanaka, S. Ichikawa, T. Hirai, J. Am. Chem. Soc. 138 (2016) 10019–10025;
(c) S. Zhao, X. Zhao, H. Zhang, J. Li, Y. Zhu, Nano Energy 35 (2017) 405–414.
[6] (a) A.J. Hoffman, E.R. Carraway, M.R. Hoffmann, Environ. Sci. Technol. 28 (1994) 776–785;
(b) S. Li, G. Dong, R. Hailili, L. Yang, Y. Li, F. Wang, Y. Zeng, C. Wang, Appl. Catal. B: Environ. 190 (2016) 26–35;
(c) L. Yang, G. Dong, D.L. Jacobs, Y. Wang, L. Zang, C. Wang, J. Catal. 352 (2017) 274–281.
[7] (a) H. Wang, L. Zhang, Z. Chen, J. Hu, S. Li, Z. Wang, J. Liu, X. Wang, Chem. Soc. Rev. 43 (2014) 5234–5244;
(b) X. Meng, L. Liu, S. Ouyang, H. Xu, D. Wang, N. Zhao, J. Ye, Adv. Mater. 28 (2016) 6781–6803;
(c) D. Lu, G. Zhang, Z. Wan, Appl. Surf. Sci. 358 (2015) 223–230;
(d) Z. Wan, G. Zhang, X. Wu, S. Yin, Appl. Catal. B: Environ. 207 (2017) 17–26.
[8] (a) N. Karousis, N. Tagmatarchis, Chem. Rev. 110 (2010) 5366–5397;
(b) M.F.L. De Volder, S.H. Tawfick, R.H. Baughman, A.J. Hart, Science 339 (2013) 535–539.
[9] (a) L. Ge, C. Han, Appl. Catal. B: Environ. 117–118 (2012) 268–274;
(b) Y. Xu, H. Xu, L. Wang, J. Yan, H. Li, Y. Song, L. Huang, G. Cai, Dalton Trans. 42 (2013) 7604–7613;
(c) T.Y. Ma, S. Dai, M. Jaroniec, S.Z. Qiao, Angew. Chem. 126 (2014) 7409–7413. Angew. Chem. Int. Ed. 53 (2014) 7281–7285;
(d) Y. Chen, J. Li, Z. Hong, B. Shen, B. Lin, B. Gao, Phys. Chem. Chem. Phys. 16 (2014) 8106–8113.
[10] (a) Y. Ji, L. Huang, J. Hu, C. Streb, Y.F. Song, Energy Environ. Sci. 8 (2015) 776–789;
(b) S.S. Wang, G.Y. Yang, Chem. Rev. 115 (2015) 4893–4962.
[11] X. Lu, K. Xu, P. Chen, K. Jia, S. Liu, C. Wu, J. Mater. Chem. A 2 (2014) 18924–18928.
[12] Y. Ji, J. Hu, L. Huang, W. Chen, C. Streb, Y.F. Song, Chem. Eur. J. 21 (2015) 6469–6474.
[13] J. Ming, Y. Wu, Y. Yu, F. Zhao, Chem. Commun. 47 (2011) 5223–5225.
[14] A. Gromov, S. Dittmer, J. Svensson, O.A. Nerushev, S.A. Perez-García, L. Licea-Jiménez, R. Rychwalski, E.E.B. Campbell, J. Mater. Chem. 15 (2005) 3334–3339.
[15] (a) H. Sheng, H. Ji, W. Ma, C. Chen, J. Zhao, Angew. Chem. 125 (2013) 9868–9872. Angew. Chem. Int. Ed. 52 (2013) 9686–9690;
(b) Y. Liu, H. Liu, C. Wang, S.X. Hou, N. Yang, Environ. Sci. Technol. 47 (2013) 13889–13895.
[16] (a) S. Obregón, Y. Zhang, G. Colón, Appl. Catal. B: Environ. 184 (2016) 96–103;
(b) Z. Wei, D. Liu, W. Wei, X. Chen, Q. Han, X. Ma, Y. Zhu, ACS Appl. Mater. Interfaces 9 (2017) 15533–15540.
[17] W. He, H. Jia, J. Cai, X. Han, Z. Zheng, W.G. Wamer, J.J. Yin, J. Phys. Chem. C 120 (2016) 3187–3195.
[18] G.P. Mane, S.N. Talapaneni, K.S. Lakhi, H. Ilbeygi, U. Ravon, K. Al-Bahily, T. Mori, D.H. Park, A. Vinu, Angew. Chem. 129 (2017) 8601–8605. Angew. Chem. Int. Ed. 56 (2017) 8481–8485.
[19] S. Kundu, Y. Wang, W. Xia, M. Muhler, J. Phys. Chem. C 112 (2008) 16869–16878.
[20] X. Wang, K. Maeda, A. Thomas, K. Takanabe, G. Xin, J.M. Carlsson, K. Domen, M. Antonietti, Nat. Mater. 8 (2009) 76–80.
[21] J. Tian, L. Zhang, X. Fan, Y. Zhou, M. Wang, R. Cheng, M. Li, X. Kan, X. Jin, Z. Liu, Y. Gao, J. Shi, J. Mater. Chem. A 4 (2016) 13814–13821.
[22] S.N. Talapaneni, S. Anandan, G.P. Mane, C. Anand, D.S. Dhawale, S. Varghese, A. Mano, T. Mori, A. Vinu, J. Mater. Chem. 22 (2012) 9831–9840.
[23] B. Zhu, P. Xia, W. Ho, J. Yu, Appl. Surf. Sci. 344 (2015) 188–195.
[24] V. Maurino, C. Minero, G. Mariella, E. Pelizzetti, Chem. Commun. (2005) 2627–2629.
[25] (a) N. Kaynan, B.A. Berke, O. Hazut, R. Yerushalmi, J. Mater. Chem. A 2 (2014) 13822–13826;
(b) H.I. Kim, O.S. Kwon, S. Kim, W. Choi, J.H. Kim, Energy Environ. Sci. 9 (2016) 1063–1073.
[26] Y. Kofuji, S. Ohkita, Y. Shiraishi, H. Sakamoto, S. Tanaka, S. Ichikawa, T. Hirai, ACS Catal. 6 (2016) 7021–7029.
[27] H. Hirakawa, S. Shiota, Y. Shiraishi, H. Sakamoto, S. Ichikawa, T. Hirai, ACS Catal. 6 (2016) 4976–4982.
[28] R. Wang, K. Pan, D. Han, J. Jiang, C. Xiang, Z. Huang, L. Zhang, X. Xiang, ChemSusChem 9 (2016) 2470–2479.
[29] C. Zhao, H. Luo, F. Chen, P. Zhang, L. Yi, K. You, Energy Environ. Sci. 7 (2014) 1700–1707.
[30] R.L. Spray, K.J. McDonald, K.S. Choi, J. Phys. Chem. C 115 (2011) 3497–3506.
[31] (a) B. Li, Y. Zhao, S. Zhang, W. Gao, M. Wei, ACS Appl. Mater. Interfaces 5 (2013) 10233–10239;
(b) J. Liu, Y. Liu, N. Liu, Y. Han, X. Zhang, H. Huang, Y. Lifshitz, S.T. Lee, J. Zhong, Z. Kang, Science 347 (2015) 970–974.